Volume 12
Number 20
21 October 2025
Pages 8219–8758

Materials Horizons

rsc.li/materials-horizons

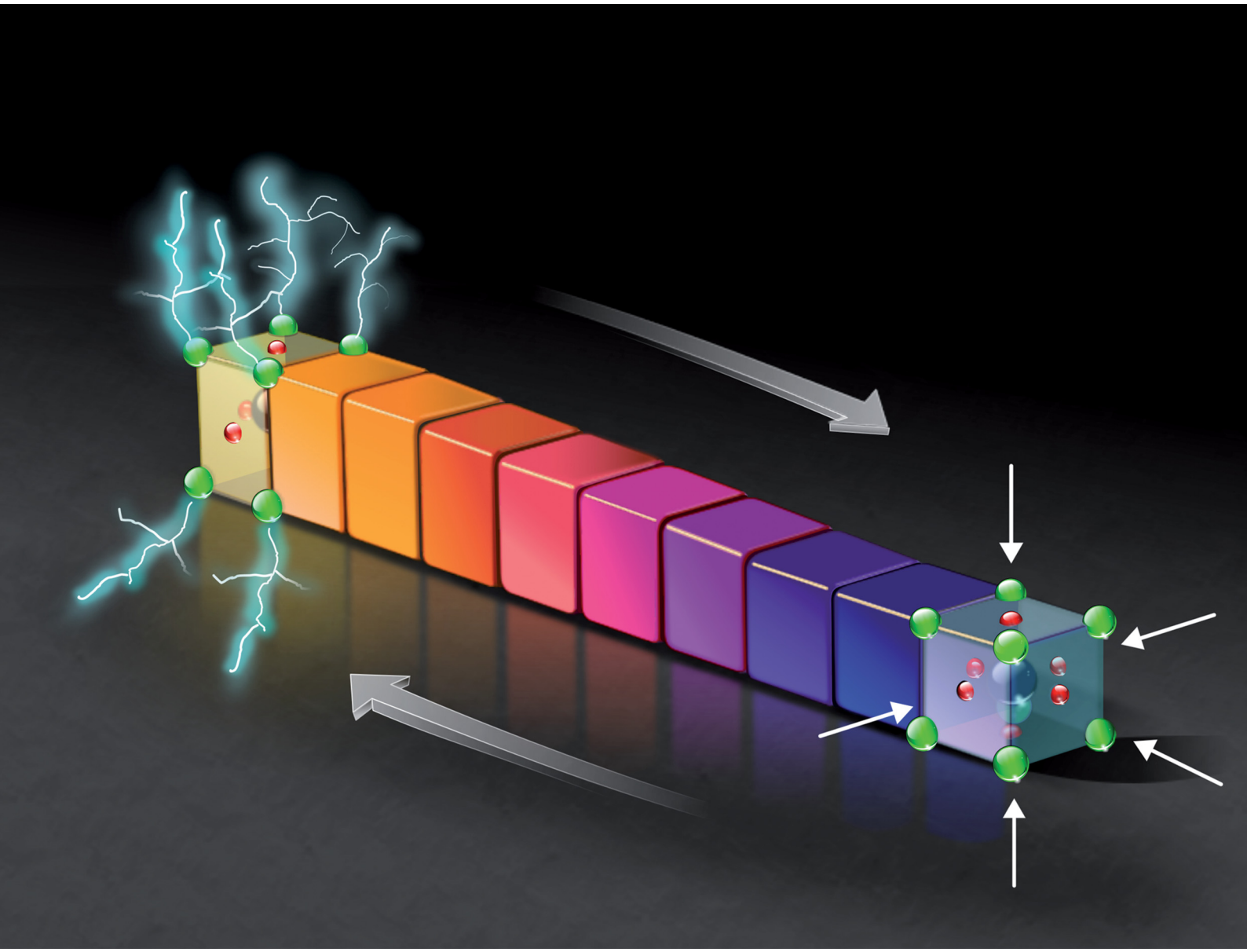

ISSN 2051-6347

ROYAL SOCIETY OF CHEMISTRY

COMMUNICATION

Àlvar Torelló, Pol Lloveras *et al.*

Simultaneous shifts in pressure and electric field boost the caloric response in ferroelectrics

Materials Horizons

ROYAL SOCIETY OF CHEMISTRY

COMMUNICATION

View Article Online
View Journal | View Issue

Cite this: *Mater. Horiz.*, 2025, **12**, 8460

Received 1st February 2025,
Accepted 30th June 2025

DOI: 10.1039/d5mh00196j

rsc.li/materials-horizons

Simultaneous shifts in pressure and electric field boost the caloric response in ferroelectrics†

Ming Zeng, [a] Michela Romanini, [a] Ivana Gorican, [bc] Silvo Drnovsek, [b] Hana Ursic, [bc] Alejandro Salvatori, [a] María Barrio, [a] Sophie Loehle, [d] Nicolas Obrecht, [d] Carlos Escorihuela-Sayalero, [a] Claudio Cazorla, [a] Àlvar Torelló, *[a] Pol Lloveras *[a] and Josep-Lluís Tamarit [a]

Solid-state caloric effects driven by external fields promise sustainable cooling and heating but their implementation requires performance enhancement. Multicaloric effects, induced by multiple fields, offer unique avenues for improvement. Here, the unexplored multicaloric potential of ferroelectrics driven simultaneously by electric field and pressure is investigated. For this purpose, unprecedented experiments of dielectric spectroscopy and calorimetry under these two fields are conducted on the archetypal electrocaloric material lead scandium tantalate ceramics. This allows analysis of the pressure–electric field phase space and the cross-coupling response of this multivariable system. More importantly, the multicaloric response offers opportunities unachievable with one field: caloric effects on decompression from 250 MPa triple if an electric field of $\sim$6 kV cm^{-1} is simultaneously applied. Conversely, reversible caloric effects, unrealizable under low electric fields, reach 2 J K^{-1} kg^{-1} if a decompression from 250 MPa is simultaneously performed. Also, tuning pressure between 0 and 300 MPa shifts the caloric response to span over 20 K below room temperature, meeting household requirements. Our study not only demonstrates the viability and novelty of multivariate calorimetry and dielectric spectroscopy; more importantly, it also reveals the impact of the multicaloric response in ferroelectrics, promising new opportunities and physical insights in this broad material family.

New concepts

Our study has demonstrated two new concepts in materials science and condensed matter physics: (i) the multicaloric potential of ferroelectric compounds under simultaneous changes of pressure and electric field, which shows a significantly enhanced performance compared to the monocaloric counterparts; and, to this end, (ii) the realization of unprecedented calorimetry and dielectric spectroscopy experiments under simultaneous application of pressure and electric field. This area has been scarcely explored, mainly because only a very few experimental studies have previously addressed monocaloric effects under a secondary constant field in ferroelectric compounds; in contrast, in our study, multicaloric effects are investigated under simultaneous changes in both pressure and electric field. Our investigation demonstrates that (i) the multicaloric effects can be multiplied, (ii) the required driving fields can be reduced and (iii) the operating temperature range can be extended or shifted. Moreover, as we envision similar effects in other compounds within the broad family of ferroelectrics, our findings have implications for the understanding and development of multicaloric materials, while offering practical insights for innovative designs of next-generation cooling technologies.

1 Introduction

In recent decades, caloric effects emerging from changes in external fields have been extensively investigated for solid-state cooling and heating as a sustainable alternative to powerful greenhouse gas-emitting vapor compressors.[1] Caloric effects are categorized based on the applied field: magnetocaloric (MC), electrocaloric (EC), elastocaloric (eC) and barocaloric (BC), driven by magnetic, electric, uniaxial stress and hydrostatic pressure fields, respectively, among others. Multicaloric effects refer to the concurrent or concatenated occurrence of these monocaloric effects,[2] offering the potential for enhanced caloric performance due to additional cross-coupling contributions that arise from the response of physical properties to non-conjugate fields.[3] These improvements include broadening or shifting the operational temperature range, increasing the magnitude of the caloric effects and/or reducing the magnitude of the required field strength. A well-known example of the

[a] *Group of Characterization of Materials, Department of Physics and Barcelona Research Center in Multiscale Science and Engineering, Universitat Politècnica de Catalunya, Av. Eduard Maristany 16, 08019, Barcelona, Catalonia, Spain. E-mail: pol.lloveras@upc.edu, alvar.torello@upc.edu*
[b] *Electronic Ceramics Department, Jozef Stefan Institute, Jamova Cesta 39, 1000 Ljubljana, Slovenia*
[c] *Jozef Stefan International Postgraduate School, Jamova Cesta 39, 1000 Ljubljana, Slovenia*
[d] *TotalEnergies OneTech, 69360, Solaize, France*

† Electronic supplementary information (ESI) available. See DOI: https://doi.org/10.1039/d5mh00196j

latter improvement is the ability to circumvent the threshold field imposed by the transition hysteresis[4] through the application of a secondary field.[5] In turn, magnetic fields lowered down to 2 T can be generated by permanent magnets; lower hydrostatic pressures allow the decrease of wall thicknesses holding pressure gradients, which decreases costs and improves the heat exchange rate and therefore the operational frequency; lower non-hydrostatic stresses mitigate issues related to fatigue; lower applied electric fields may avoid leakage current and dielectric loss issues, and facilitate the use of thick films with large thermal masses instead of multilayer capacitors.

The aforementioned opportunities have now sparked growing interest in the field of multicalorics, yet much remains unexplored due to the complexity involved in practical implementation.[6] In single compounds, multicaloric effects maintaining one field constant have been investigated by combining magnetic or electric fields with pressure or uniaxial stress.[7–13] Instead, simultaneous changes in multiple fields have been experimentally considered only by combining magnetic field and pressure.[14] However, the combination of electric field and pressure changes is promising because it could benefit from the strong cross-coupling between concomitant changes in volume and polarization at ferroelectric (FE) transitions. Such changes are coupled because both emerge from the same physical phenomena: spontaneous ionic displacements that are linked to atomic orbital hybridization and long-range electrostatic interactions (*e.g.* dipole–dipole). Therefore, electric field and pressure each will individually drive changes in volume and polarization, resulting in cross-coupling effects. In fact, significant BC and/or EC effects have been reported independently in a variety of FE materials, including traditional FE inorganic salts,[15–19] FE polymers[20,21] and novel FE hybrid organic–inorganic plastic crystals.[22] Additionally, FE compounds are often composed of abundant and inexpensive elements, and electric fields are easier and less costly to generate than large magnetic fields. These features further support the potential of multicaloric effects driven by simultaneous changes in electric field and pressure, but to date, only a few theoretical studies have addressed this matter.[23,24]

The present work addresses unprecedented experiments of calorimetry and dielectric spectroscopy under simultaneous electric field and pressure on FE materials. As a proof of concept, we study the well-known FE and pyroelectric oxide lead scandium tantalate (PST), which currently enjoys technological applications as a thermal detector.[25] This material is also a relevant EC agent[26,27] and has been used in high-performance EC cooling devices.[28,29] With our experiments, we provide direct physical insights and functional opportunities associated with the thermodynamics of the multidimensional temperature–pressure–electric field phase space. In particular, we demonstrate that the overall caloric performance of PST can be significantly enhanced under the simultaneous application of two different fields. Furthermore, a constant pressure within the range of 0–300 MPa can shift the operational temperature range below room temperature and expand the reversibility regime, which are two key requirements for large-scale applications. Our study not only demonstrates relevant multicaloric performance improvements and experimental feasibility of these novel techniques but also opens up the door to investigating a wide range of FE compounds in a similar fashion for future solid-state coolers.

2 Methods

2.1 Material synthesis and structural characterization

PbO (product no. 12220, Alfa Aesar, USA), Sc_2O_3 (product no. 11216, Alfa Aesar, USA) and Ta_2O_5 (product no. 73118, Alfa Aesar, USA) were used to synthesize the PST powder. The homogenized stoichiometric mixture was mechanochemically activated in a high-energy planetary mill (model: PM 400, Retsch, Germany) with 15 WC balls ($2r$ = 20 mm) in a 250 ml WC vessel for 24 h at 300 rpm. The powder was then heated at 1000 °C for 2 h in a closed aluminum oxide crucible. The synthesized powder was milled in an attrition mill with yttria-stabilized zirconia (YSZ) balls in isopropanol at 800 min^{-1} for 4 h to achieve deagglomeration. The powder was then uniaxially pressed into cylindrical pellets and further consolidated by isostatic pressing at 300 MPa (Autoclave Engineers, USA). The powder compacts were sintered at 1300 °C for 2 hours and annealed at 1000 °C for 48 hours to achieve a high order of B-site ions inside the pellets. This thermal treatment of the pellets was carried out in the packing powder, which consisted of $PbZrO_3$ with the addition of 2 mol% PbO powder in excess. The density of the ceramics was measured using a gas displacement density analyzer (AccuPyc II1340 Pycnometer, Micromeritics, USA). The density of the pellets reached 96.5% of the theoretical density. The theoretical density value was determined from line card no. 00-043-0134 of the powder sample analysis program X'Pert HighScore Plus (PANalytical B. V., The Netherlands).

2.2 Calorimetry

Differential scanning calorimetry was conducted using a DSC Q100 (TA Instruments), with different scanning rates in the range of 2–10 K min^{-1}. For this purpose, small pieces of ~50 mg were cut from sintered disks and encapsulated in aluminum pans.

Differential thermal analysis (DTA) under pressure and electric field was performed using an MV1-30 high-pressure cell (Unipress, Poland), which can operate up to 0.6 GPa and between 200 K and 393 K, equipped with an upper closure that allows multiple electric signals to pass through. The PST sample was a disk with 15.1 mm diameter and 1.4 mm thickness. Cu wires were attached to Au electrodes deposited on PST faces using an RF-magnetron sputtering machine (5 Pascal, Italy). Peltier modules were used as calorimetric sensors and type T thermocouples were placed near the sample to monitor temperature. A high-voltage power supply (model: HPX-20-757-152, ISEG Spezialelektronik GmbH) able to deliver 2000 V and 750 mA (hence 1500 W) was used to generate electric fields applied to the sample. To account for any possible influence of the pressure-transmitting fluid and Peltier sensors under pressure, calibration of the calorimetric signal was performed using several Cu-based alloys undergoing isochoric (shear-based) transitions at different temperatures as calibrants. These alloys

were measured at different pressures and, due to the isochoric character of the phase transitions, any dependence of the caloric peak integrals on pressure was used to calculate the pressure- and temperature-dependent sensitivity function required to correct the calorimetric signal. A schematic of the experimental setup is shown in Fig. S1a (ESI†).

2.3 Dielectric spectroscopy

Pressure- and electric field-dependent dielectric spectroscopy (DS) measurements were carried out using a parallel-plate capacitor containing a PST disk of 16.3 mm diameter and 0.194 mm thickness as the dielectric material. In order to prevent possible contamination by the pressurizing fluid (thermal oil from Huber), the capacitor was covered with a Teflon membrane and latex wrapping. The insulated capacitor was then placed inside a high-pressure chamber (Unipress) made of a Cu–Be alloy, which was filled with the thermal oil and connected to a manual pump that allowed applying a hydrostatic pressure between ambient pressure and 600 MPa (measured with a pressure transducer with an accuracy of ±0.5%). The measurements were performed using a Novocontrol Alpha Analyzer connected to an HVB300 high-voltage booster that can provide a DC output voltage of 300 V_{pp}. The temperature was controlled by a thermal bath (Lauda Proline RP 1290) with a liquid-flow circuit connected to a high-pressure setup. The real part of the dielectric permittivity at a fixed frequency of 100 Hz was measured every 20 s during cooling and heating ramps at different values of pressure and applied voltage. The temperature ramps were done at a rate of 1 K min^{-1} in the temperature range between 263 and 323 K. The range of pressures applied was between 0 and 200 MPa, and the applied voltage varied between 0 and 140 V. In both DTA and DS measurements, we estimate the thickness of the sample to shrink no more than ~0.5%, given the bulk modulus of similar materials (~50–200 GPa) and the maximum applied pressure (~0.4 GPa). A schematic of the experimental setup is shown in Fig. S1b (ESI†).

2.4 Computational methods

The vibrational properties of paraelectric $Pb(Sc_{0.5}Ta_{0.5})O_3$ were calculated with first-principles methods based on density functional theory (DFT). We used the PBEsol variant of generalised gradient approximation to DFT[30] as it is implemented in the VASP package.[31,32] The ''projector augmented wave'' method was employed to represent the ionic cores,[33] and the following electrons were considered as valence: Pb 6s and 6p; Ta 6s and 5d; Sc 4s and 3d; and O 2s and 2p. Wave functions were represented in a plane-wave basis set truncated at 650 eV. We used a 40-atom simulation cell (Fig. S2a, ESI†), in which cationic Ta/Sc order characterizing PST and the usual polar and antiferrodistortive distortions occurring in oxide perovskites could be reproduced.[34–36] For integrations within the first Brillouin zone, we adopted a Gamma-centred *k*-point grid of 8 × 8 × 8. Geometry relaxations were performed using a conjugate-gradient algorithm that optimized the volume and shape of the simulation cell as well as the atomic positions. The imposed tolerance on the atomic forces was 0.005 eV $Å^{-1}$. By using these parameters, we obtained total energies that were converged to within 0.5 meV per formula unit.

Phonons were estimated with the small displacement method[37,38] using PHONOPY software.[39] Large 2 × 2 × 2 supercells containing 320 atoms were employed in the phonon calculations. The polarity of each phonon mode appearing at the center of the Brillouin zone was estimated with the formula:

$$P_i = \sum_{jk} Z^*_{ijk} u_{jk} \quad (1)$$

where index *j* runs over all the atoms in the unit cell, indexes *i* and *k* represent Cartesian directions, u_{jk} is the phonon displacement component of the *j*-th atom in the *k* direction, and Z^*_{ijk} is the Born effective charge tensor. Polar (nonpolar) eigenmodes are characterized by non-zero (null) phonon polarity components.

3 Results and discussion

Above room temperature, lead scandium tantalate, with the chemical formula $Pb(Sc_{0.5}Ta_{0.5})O_3$ (PST for short), adopts a perovskite structure with O anions forming octahedra with Sc or Ta cations in their centers. If the occupation of Sc and Ta along the lattice is fully disordered, PST exhibits a $Pm\bar{3}m$ structure and displays a relaxor behavior with short-range polar domains developing well above room temperature.[40,41] Through long annealing times at high temperature, these cations achieve ordered arrangement, leading to a doubling of the lattice parameters with $Fm\bar{3}m$ symmetry;[42] on cooling below room temperature, ordered PST displays a weakly first-order phase transition (FOPT) towards a long-range ordered FE rhombohedral phase with *R*3 symmetry.[43] At the atomic scale, the emergence of a spontaneous polarization of $\Delta P_t \approx 20$ μC cm^{-2} at the transition is mainly associated with large and collective displacements of Pb and O ions.[26] The reduction to *R*3 symmetry across a first-order phase transition also requires octahedral tilting.[43] To further investigate the atomistic mechanisms driving the polar-to-nonpolar phase transition in PST, we performed first-principles calculations characterizing its high-temperature paraelectric cubic phase (space group: $Fm\bar{3}m$, Fig. S2a, ESI;† Methods). Specifically, using density functional theory (DFT), we computed the full phonon spectrum of PST in this centrosymmetric phase (Fig. S2b, ESI†). As observed in many prototypical oxide perovskites (*e.g.*, $BaTiO_3$ and $PbTiO_3$),[44] the phonon dispersion of the high-symmetry paraelectric phase exhibits multiple vibrational instabilities in the form of imaginary phonon branches (Fig. S2b, ESI†). These phonon instabilities serve as signatures of order parameters that condense into lower-symmetry polar phases at reduced temperatures. Such instabilities include optical polar eigenmodes, which can give rise to ferroelectricity, as well as antiferrodistortive modes associated with oxygen octahedral tilting.

At the Brillouin zone center (Γ), we identified a total of 24 imaginary frequency phonon modes in paraelectric PST. Among these, only three, corresponding to an energy-degenerate set, were polar. The lowest-frequency imaginary

phonon mode (−20.5 meV) corresponds to a nonpolar antiferrodistortive mode characterized by out-of-phase oxygen octahedral rotations (Fig. S2c, ESI†). In contrast, the degenerate polar phonon mode, with an imaginary frequency of −13.3 meV, involves large displacements of Pb and O atoms in opposite directions, while Sc and Ta exhibit negligible off-center shifts (Fig. S2d, ESI†). The atomic arrangement associated with this imaginary polar phonon mode is consistent with the off-center displacements observed experimentally in ferroelectric PST.[45]

In PST, coupling between both primary order parameters, *i.e.* octahedral tilting and polarization, is mediated by strain. Therefore, strain is a secondary order parameter so that the FE transition is also improper ferroelastic.[46] This displacive deformation, also involving distortion of the octahedra, is mainly shear-based as indicated by the elastic softening of the shear modulus but also carries a positive unit cell volume change of $\Delta V_t \approx 0.078$ Å^3.[43] This allows the FE transition to be driven by applying an electric bias and the inverse transformation by increasing hydrostatic pressure. Indeed, additional pressure-dependent DFT phonon calculations reveal a noticeable increase in the frequency of the imaginary polar Γ-point phonon mode upon a pressure increase, which anticipates the pressure-driven stabilization of the paraelectric phase (see the discussion above). Specifically, the pressure derivative of this vibrational mode is found to be $d\omega/dp$ = 0.08 meV GPa^{-1}, and the corresponding Grüneisen parameter, defined as $\gamma = -(V/\omega)(d\omega/dV)$, is calculated to be 1.12. Therefore, EC, BC, and hence multicaloric effects can be harvested.

X-ray powder diffraction patterns of our PST ceramics conducted at room temperature indicate a large degree of ordering $\Omega \simeq 0.87$ determined as the ratio between (111) and (200) peaks[43] (see Section S3 of the ESI† for the structural and microstructural analyses). Differential scanning calorimetry (DSC) performed at atmospheric pressure under no applied electric field yielded signals corresponding to the expected FOPT. DSC measurements at different scanning rates (see Fig. S4a, ESI†) show that the transition temperature (regardless of taking the peak onset or the peak maximum) and peak width varies only slightly when significantly changing the temperature rate (Fig. S4b, ESI†), which is indicative of a marked athermal character.[47] Therefore, the transition hysteresis can be considered as nearly intrinsic to the material and independent of the temperature rate over a wide range of conditions. More importantly, this feature allows the field-induced transition hysteresis to be directly deduced from the temperature-induced transition hysteresis. Integrals of the peak yielded entropy and enthalpy changes at the transition. Using scanning rates of ∼5–10 K min^{-1} as a standardized protocol, reliable values of $\Delta H_t \simeq 0.9$ J g^{-1} (Fig. S4c, ESI†) and $\Delta S_t \simeq 3$ J K^{-1} kg^{-1} are obtained, which are in agreement with the literature for PST samples with a similar degree of ordering.[2,27,40,41]

3.1 Calorimetry and dielectric spectroscopy under applied pressure and electric field

Dielectric spectroscopy (DS) and differential thermal analysis (DTA) experiments were performed under temperature scan and subjected to different constant pressures p and electric fields E simultaneously (see Fig. 1(a) and (b), respectively, for selected measurements, and Fig. S5, ESI,† for the full set of DTA measurements). The obtained DS and DTA signals exhibit peaks in dielectric permittivity (ε') and in heat flow $\left(\frac{dQ}{|dT|}\right)$, respectively, associated with the FOPT. The values of ε' are in agreement with reported literature values with no applied pressure.[27,48–50] DTA peaks become sharper with increasing electric field and weaken with increasing pressure so that at very high pressures and low electric fields the peaks become undetectable. This is consistent with a strong decrease of the transition entropy changes ΔS_t with pressure, calculated by integrating peaks in $\frac{dQ}{T dT}$ after baseline subtraction. In contrast, ΔS_t is roughly independent of the applied electric field within the range studied here. In particular, we find ΔS_t (p = 400 MPa, E) ≈ 0.5 J K^{-1} kg^{-1} (see Fig. S6, ESI†).

The transition temperatures were determined from the peak maximums in both DS and DTA signals, which are consistent with each other within uncertainty. These data allowed us to calculate the endothermic and exothermic transition surfaces as a function of p and E, and therefore the 3-dimensional phase diagram $T(p,E)$ (see Fig. 1(c) for the 3-dimensional representation and Fig. S7, ESI,† for projections on the $T(p)$ and $T(E)$ planes). It can be seen that the applied pressure and the electric field shift the FOPT towards lower and higher temperatures, respectively, consistent with the positive changes in volume and polarization at the exothermic transition, and anticipating inverse BC and conventional EC effects. At E = 0 and atmospheric pressure (p_{atm}), we observe that the endothermic transition temperature depends on pressure as $\left(\frac{\partial T}{\partial p}\right)_{E=0,p_{atm}} \simeq -46$ K GPa^{-1}. This value is in agreement with the value calculated *via* the Clausius–Clapeyron (CC) equation $\left(\frac{\partial T}{\partial p}\right)_E = \frac{\Delta V_t}{\Delta S_t} = -43$ K GPa^{-1}. This value remains nearly constant up to $p \lesssim 250$ MPa, above which its absolute value increases continuously so that at p = 300 MPa we obtain $\left(\frac{\partial T}{\partial p}\right)_{E=0,p=300\ \mathrm{MPa}} \simeq -175.5$ K GPa^{-1}. This is consistent with the aforementioned strong decrease of ΔS_t with pressure and ΔV_t independent of pressure. The values for $\left(\frac{\partial T}{\partial p}\right)_{E,p}$ are found to be roughly independent of the applied electric field. On the other hand, at any constant E the exothermic surface shows a steeper slope than the endothermic surface, and hence the transition hysteresis increases with increasing pressure. In turn, the temperature–electric field transition line at normal pressure shows slight concavity at very low values of the applied field and rapidly becomes linear with a slope $\left(\frac{\partial T}{\partial E}\right)_{p_{atm}} \simeq 0.55$ K cm kV^{-1}, in agreement with the literature[27] but below the Clausius–Clapeyron value $\left(\frac{\partial T}{\partial E}\right)_{p_{atm}} = -\frac{\Delta P_t}{\rho \Delta S_t} \sim 0.7$ K cm kV^{-1} ($\rho \approx 9000$ kg m^{-3} is density). This discrepancy may be due to the imperfect degree of ordering and the polycrystalline -nature of the sample; a thorough

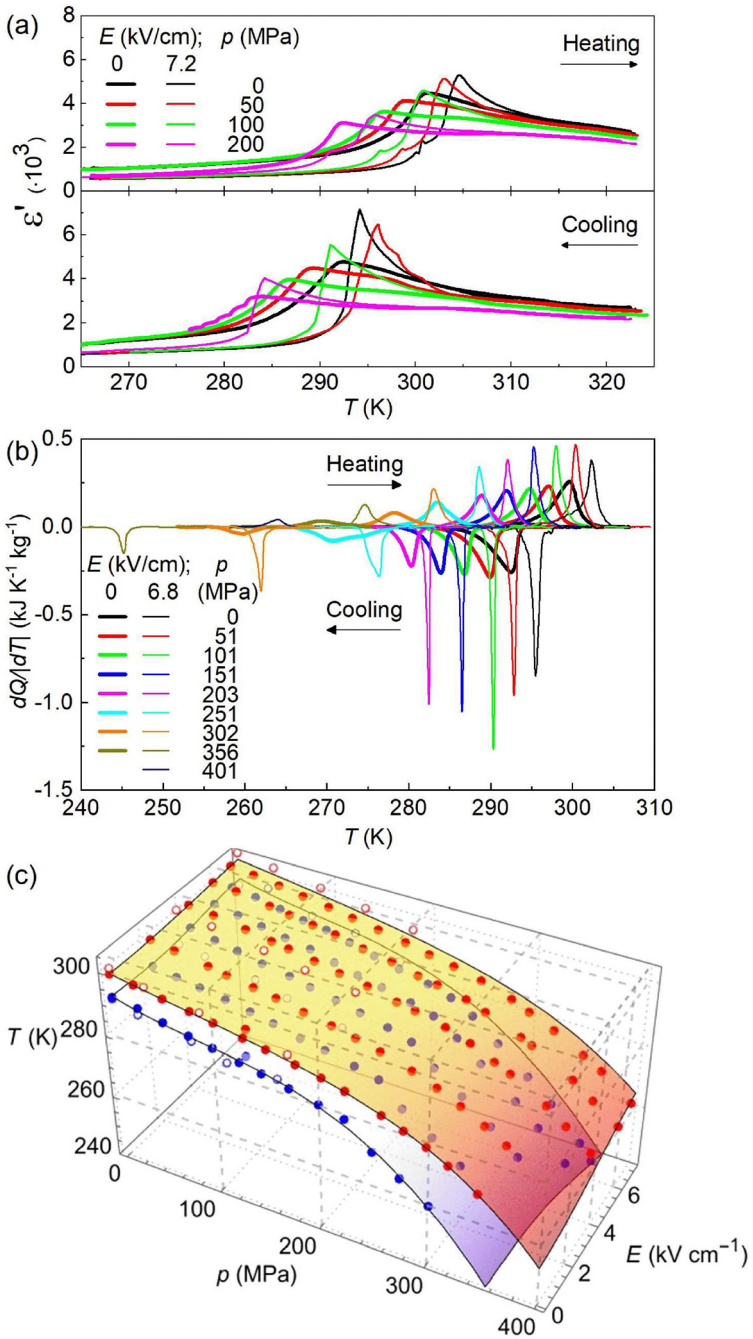

Fig. 1 (a) Dielectric permittivity and (b) thermograms as a function of temperature for different values of applied pressure and electric field upon heating and cooling across the transition. (c) $T(p,E)$ phase diagram. Empty symbols are determined from (a) and solid symbols and surfaces are determined from (b). Red and blue colors stand for endothermic and exothermic data, respectively. Surfaces are smooth polynomial fits to the data.

investigation is however beyond the scope of this work. Additionally, under isothermal conditions, we find that the transition pressure depends on the electric field as $\frac{dp}{dE} \sim 120\ \mathrm{C\ m^{-2}}$, which is in reasonable agreement with the multivariate Clausius–Clapeyron equation $\frac{dp}{dE} = \frac{\Delta P_t}{\rho \Delta V_t} \sim 170\ \mathrm{C\ m^{-2}}$.

The isofield DTA measurements were used to calculate the multicaloric effects using the quasi-direct method. For this purpose, the entropy curves $S(T,p,E)$ were determined with respect to a reference value $S_0 = S(T_0,p_{atm},0)$ using the following equation:

$$S(T,p,E) = S_0 + \int_0^T \frac{1}{T'}\left(C_p + \frac{dQ}{dT'}\right)dT' - \int_{p_{atm}}^{p}\left(\frac{\partial V}{\partial T}\right)_{p',E} dp' + \int_0^E \frac{1}{\rho}\left(\frac{\partial P}{\partial T}\right)_{p,E'} dE' \quad (2)$$

Here $\frac{dQ}{dT}$ is the measured p- and E-dependent DTA heat flow accounting for the entropy change at the transition (see Fig. 1(b)) and C_p is the heat capacity at constant fields. The last two terms account for additional entropy changes arising in individual phases due to temperature-dependent volume V and polarization P. Within the range of the applied fields in this study, these terms are small compared to the other terms[43,51] and were neglected. Full calculation details are given in Section S6 and Fig. S8 of the ESI,† and the resulting entropy functions are displayed in Fig. S9 (ESI†). Subsequently, multicaloric effects were calculated by subtracting entropy functions at different applied p and E:

$$\Delta S(T,p_0 \rightarrow p_1,E_0 \rightarrow E_1) = S(T,p_1,E_1) - S(T,p_0,E_0) \quad (3)$$

$$\Delta T(T_s,p_0 \rightarrow p_1,E_0 \rightarrow E_1) = T(S,p_1,E_1) - T_s(S,p_0,E_0) \quad (4)$$

where ΔT is conveniently expressed as a function of the starting temperature T_s because the temperature changes during the process. From now on, the smaller field during a field change will always be $E = 0$ and $p = p_{atm} \simeq 0$ unless otherwise specified.

3.2 Monocaloric effects under a secondary constant field

As the simplest situation, we first consider the monocaloric effects obtained by varying one field while keeping the other constant, *i.e.* BC effects under constant E or EC effects under constant p. This behavior is illustrated in Fig. 2. Fig. 2(a) and (b) display isofield entropy curves as a function of temperature for selected values of p and E: $p = 0, E = 0$ (solid orange line); $p = 150$ MPa, $E = 0$ (solid green line); $p = 0, E = 6.8$ kV cm^{-1} (dotted orange line); and $p = 150$ MPa, $E = 6.8$ kV cm^{-1} (dotted green line). Vertical and horizontal arrows represent monocaloric effects (ΔS and ΔT, respectively) driven by a compression of $0 \rightarrow 150$ MPa at constant $E = 6.8$ kV cm^{-1} (Fig. 2(a)) and an increase in the electric field of $0 \rightarrow 6.8$ kV cm^{-1} at constant $p = 150$ MPa (Fig. 2(b)). Fig. 2(c) and (e) show ΔS and ΔT, respectively, under first compression of $0 \rightarrow 150$ MPa, under different constant E values. It can be observed that, as the applied electric field increases, the operational temperature range of the BC effects shifts to higher temperatures, as expected. The opposite scenario, featuring EC effects under constant p, is presented in Fig. 2(d) and (f). Similar qualitative characteristics to those observed in the previous case are observed, though quantitatively reversed: as the applied pressure increases, the operational temperature range shifts to lower values, as expected. In this case, the magnitudes of both $|\Delta S|$ and $|\Delta T|$ decrease slightly with increasing p due to the dependence of the transition entropy change on p (see Fig. S6, ESI†).

From Fig. 2(c)–(f), it can be observed that the maximum $|\Delta S|$ and $|\Delta T|$ for both BC and EC effects are $\sim$2.5 J K^{-1} kg^{-1} and $\sim$2.5 K, respectively. These values agree with the literature[27,43,46] and are consistent with the equation relating

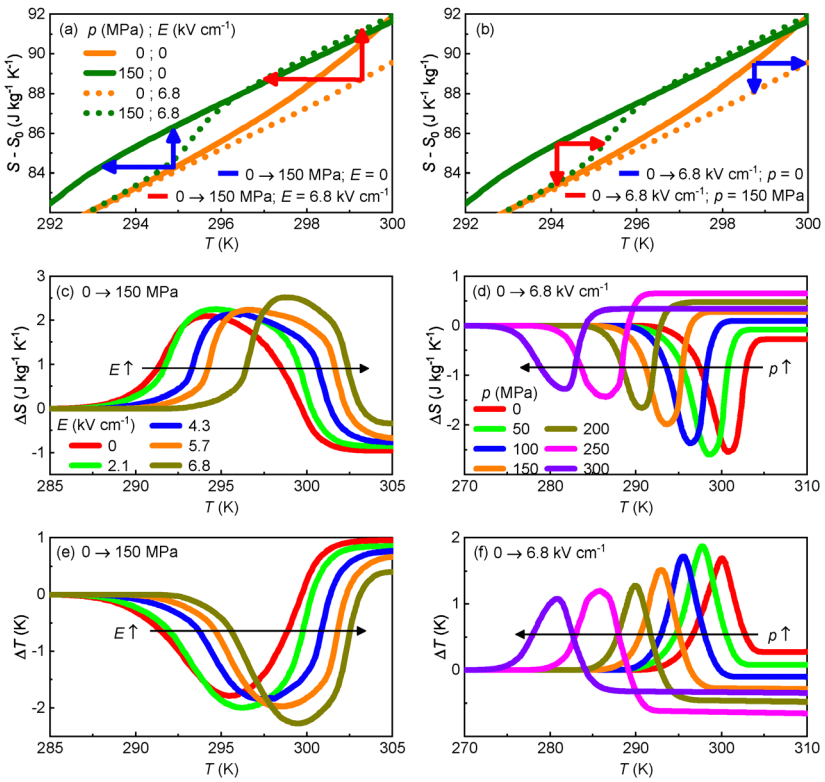

Fig. 2 Monocaloric effects under additional constant fields. (a) and (b) Isofield entropy curves as a function of temperature for different values of p and E. (c) and (d) Isothermal entropy changes and (e) and (f) adiabatic temperature changes driven by (c) and (e) Δp under constant E and driven by (d) and (f) ΔE under constant p. Legends in panels (a), (c) and (d) also hold for panels (b), (e) and (f), respectively. Arrows in panels (c)–(f) represent the shift direction with increasing field change.

both quantities $\Delta T = -(T/C_p)\Delta S$. While this equation is strictly valid for a homogeneous thermodynamic system (*i.e.* for a single phase), in the case of PST it appears to be a good approximation due to the weak first-order character of the transition.

Moreover, notice that BC effects (see Fig. 2(c) and (e)) associated with the phase transition are inverse (*i.e.* a compression results in $\Delta S > 0$ and $\Delta T < 0$) because the volume change at the endothermic transition is negative. Instead, above the phase transition the BC effects change in sign and become conventional (*i.e.* a compression results in $\Delta S < 0$ and $\Delta T > 0$) due to positive thermal expansion of the paraelectric phase. In the ferroelectric phase, the thermal expansion is smaller, which results in approximately negligible effects. Regarding the EC effects (see Fig. 2(d) and (f)), they are conventional at the transition because polarization decreases across the endothermic transition. In the paraelectric phase, under low or moderate constant pressures, the EC effects are negligible because polarization is zero and independent of temperature. However, at very high constant pressures, the obtained EC effects are not reliable due to the accumulation of experimental uncertainties.

3.3 Non-synergetic multicaloric effects

Since this material exhibits conventional EC effects and inverse BC effects across the transition, changes in p (Δp) and E (ΔE) with the same sign ($\Delta p \cdot \Delta E > 0$, in-phase) produce monocaloric contributions that are opposite in sign. Consequently, these non-synergetic contributions subtract each other when combined in multicaloric effects resulting in a reduced overall response compared to the individual monocaloric responses. In contrast, the magnitudes of $|\Delta S|$ and $|\Delta T|$ can be maximized by increasing one field while decreasing the other ($\Delta p \cdot \Delta E < 0$, antiphase). This behavior is illustrated in Fig. 3 using heating data only for clarity. Fig. 3(a) and (b) display isofield entropy curves as a function of temperature for selected values of p and E: $p = 0$, $E = 0$ (solid orange line), $p = 150$ MPa, $E = 0$ (solid green line), $p = 0$, $E = 6.8$ kV cm^{-1} (dashed orange line) and $p = 150$ MPa, $E = 6.8$ kV cm^{-1} (dashed green line). Vertical and horizontal arrows stand for ΔS and ΔT, respectively. In Fig. 3(a), red, blue and black arrows indicate monocaloric effects driven by $\Delta p > 0$, monocaloric effects driven by $\Delta E > 0$ and multicaloric effects driven by simultaneous $\Delta p > 0$ and $\Delta E > 0$, respectively. In Fig. 3(b), red, blue and black arrows stand for monocaloric effects driven by $\Delta p > 0$, monocaloric effects driven

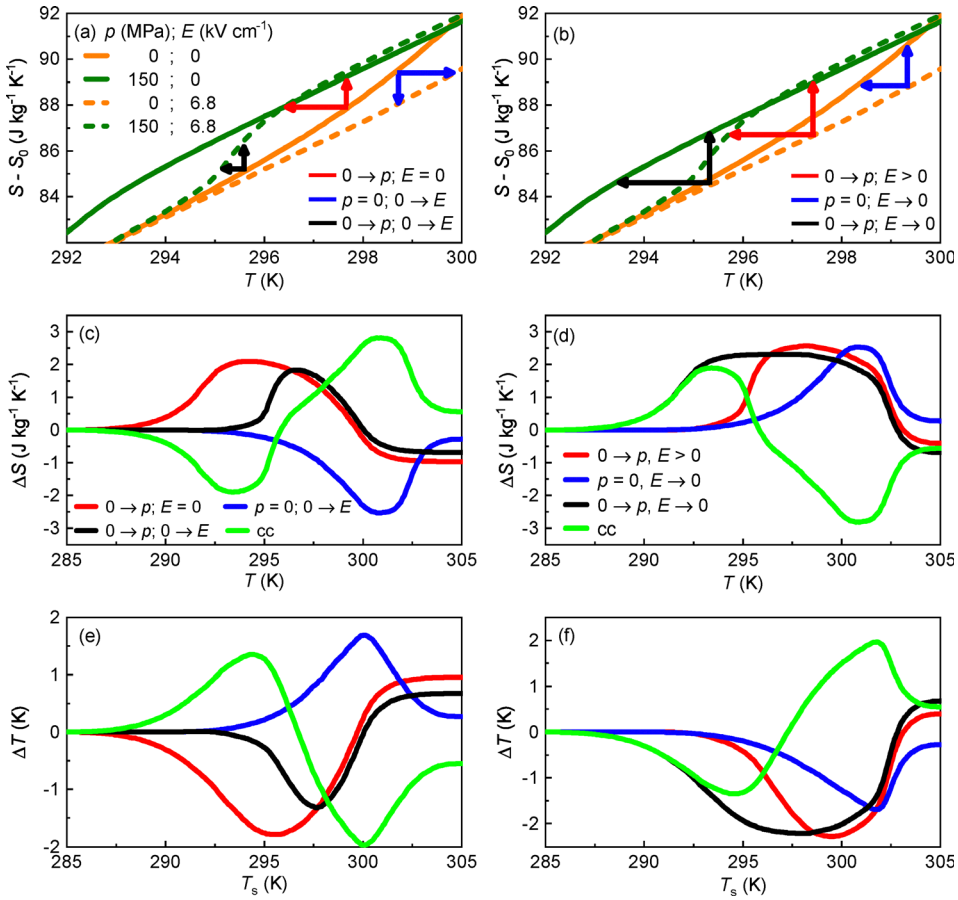

Fig. 3 Multicaloric effects and cross-coupling contributions. (a) and (b) Isofield entropy curves as a function of temperature for the same selected values of applied pressure and electric field in both panels. Red and blue arrows denote caloric effects associated with monocaloric effects. Black arrows denote multicaloric effects driven by (a) in-phase changes of pressure and electric field and (b) antiphase changes of pressure and electric field. (c)–(f) Red and blue lines indicate monocaloric ΔS (c) and (d) and ΔT (e) and (f) driven by changes in p and E, respectively. Black lines denote in-phase (c) and (e) and antiphase (d) and (f) multicaloric effects. Green lines stand for cross-coupling contributions in each case.

by $\Delta E < 0$ and multicaloric effects driven by $\Delta p > 0$ and $\Delta E < 0$, respectively. In both panels, the multicaloric paths start at 295.5 K. The corresponding values for ΔS and ΔT are plotted as functions of temperature in Fig. 3(c) and (d) and (e) and (f), respectively, with the same color legend. These plots confirm the expected characteristics of non-synergetic multicaloric effects: the in-phase change of fields results in multicaloric effects (black curves in Fig. 3(c) and (e)) that are reduced compared to the monocaloric effects (red and blue curves in Fig. 3(c) and (e)). Conversely, the antiphase change of fields produces a multicaloric response (black curves in Fig. 3(d) and (f)) that is enhanced relative to the monocaloric effects (red and blue curves in Fig. 3(d) and (f)). A comprehensive comparison between multicaloric effects driven by in-phase and antiphase field changes is presented in Fig. S10 (ESI†).

Additionally, these results provide insight into the cross-coupling between the two degrees of freedom and the corresponding non-conjugate fields, *i.e.*, the cross-susceptibility. Relevant multicaloric effects in FEs involve the generalized coordinates V and P, along with their respective conjugate fields p and E. It can be shown that multicaloric ΔS due to changes $p_0 \rightarrow p_1$ and $E_0 \rightarrow E_1$ can be expressed as follows (see Section S7 of the ESI† for complete mathematical details):

$$\Delta S(T,p_0\rightarrow p_1,E_0\rightarrow E_1) = \Delta S(T,p_0\rightarrow p_1,E_0)+\Delta S(T,p_0,E_0\rightarrow E_1) + \int_{p_0}^{p_1}\int_{E_0}^{E_1}\left(\frac{\partial \chi_{12}}{\partial T}\right)_{p,E} \mathrm{d}p\mathrm{d}E. \quad (5)$$

The last term in eqn (5) is the cross-coupling contribution ΔS_{cc} where χ_{12} is the off-diagonal component of the cross-susceptibility symmetric tensor defined as $\chi_{12} \equiv -\frac{1}{\rho}\left(\frac{\partial P}{\partial p}\right)_{T,E} = \left(\frac{\partial V}{\partial E}\right)_{T,p}$. This equation shows that for materials with strong cross-response between generalized coordinates and non-conjugated fields, the multicaloric effects may change with respect to the summation of the monocaloric counterparts.

Following eqn (5), the cross-coupling contributions to the caloric effects can be defined as the difference between the multicaloric effects obtained when both p and E are varied simultaneously and the sum of the monocaloric effects from changing only $p_0 \rightarrow p_1$ (at E_0) and only $E_0 \rightarrow E_1$ (at p_0). Therefore, ΔS_{cc} and ΔT_{cc} can be calculated through the subtraction of the red and blue curves from the black curve and are displayed by green lines in Fig. 3(c)–(f). These contributions show positive and negative contributions, which reverse sign between in-phase and antiphase changes of fields, in agreement with the theoretical prediction.[52] A comprehensive set of ΔS_{cc} driven by different values of in-phase field changes is shown in Fig. S11 (ESI†).

3.4 Reversible multicaloric effects driven by the antiphase change of fields

The reversibility of the multicaloric effects has not been analyzed in previous sections. To include this technologically relevant feature, it is important to note that in PST transitions driven by isothermal $\Delta E > 0$ and/or $\Delta p < 0$ ($\Delta E < 0$ and/or $\Delta p > 0$) are exothermic (endothermic). Therefore, reversible multicaloric effects (ΔS_{rev} and ΔT_{rev}) driven by antiphase field changes can be calculated using the shortest path by subtracting the entropy curve obtained on isofield heating S_H at pressure p and $E = 0$ from the entropy curve obtained on isofield cooling S_C at $p = 0$ and electric field E. Mathematically:

$$\Delta S_{rev}(T,0 \rightleftarrows p,E \rightleftarrows 0) = \pm[S_H(T,p,E=0) - S_C(T,p=0,E)] \quad (6)$$

$$\Delta T_{rev}(T_s,0 \rightleftarrows p,E \rightleftarrows 0) = \pm[T(S_H,p,E=0) - T(S_C,p=0,E)] \quad (7)$$

where right (left) arrows correlate with the positive (negative) sign. These equations hold provided that the changes in p and E shift the exothermic transition to higher temperature than the endothermic transition.[4,5] Therefore, these equations highlight that, to drive reversible effects, the larger the hysteresis, the larger the required field changes. This increases the necessary work, consequently reducing the performance of the materials.

The resulting reversible effects are shown in Fig. 4. Fig. 4(a) shows ΔS_{rev} as a function of temperature for $\Delta E = -6.8$ kV cm^{-1} and different $\Delta p > 0$. The contour plot (Fig. 4(b)) shows $|\Delta S_{rev}|$ as a function of antiphase changes of p and E at 291 K. Analogous plots for ΔT_{rev} are shown in Fig. 4(c) and (d). Interestingly, the more intense colors in both contour plots indicate that multicaloric ΔS_{rev} and ΔT_{rev} are enhanced with larger changes in both fields. As a quantitative example, while reversible EC effects under a small shift of 5 $\rightarrow$ 0 kV cm^{-1} are zero and reversible BC effects under compression from atmospheric pressure to 200 MPa amount to <1 J K^{-1} kg^{-1}, multicaloric effects rise up to >2 J K^{-1} kg^{-1} if both fields are changed at the same time. Also, $|\Delta S_{rev}|$ and $|\Delta T_{rev}|$ driven by $\Delta p = 250$ MPa are more than tripled if $\Delta E = -6.8$ kV cm^{-1} is applied.

3.5 Multivariate $T(p,E)$ phase diagram and reversible cycles

To achieve a fully reversible thermodynamic cycle, the field change must be large enough to induce both endothermic and exothermic FOPTs within each cycle. Consequently, the hysteresis associated with the transition increases the required field change, which in turn decreases the efficiency of the cycle and narrows the operational temperature window. In multicaloric materials, the ability to apply more than one field enables the design of thermodynamically reversible cycles that would otherwise be irreversible if only a single field were applied. The reversibility of the caloric effects can be assessed by drawing closed paths in the $T(p,E)$ phase diagram that must cross both the endothermic and exothermic transitions. Fig. 5(a) shows two such examples in an enlarged view of the $T(p,E)$ diagram (see Fig. 1(c)) in the low-pressure region where endothermic (reddish) and exothermic (bluish) surfaces can be approximated by planes: if monocaloric effects are considered, no reversible BC effects can be obtained above $\sim$293 K for any

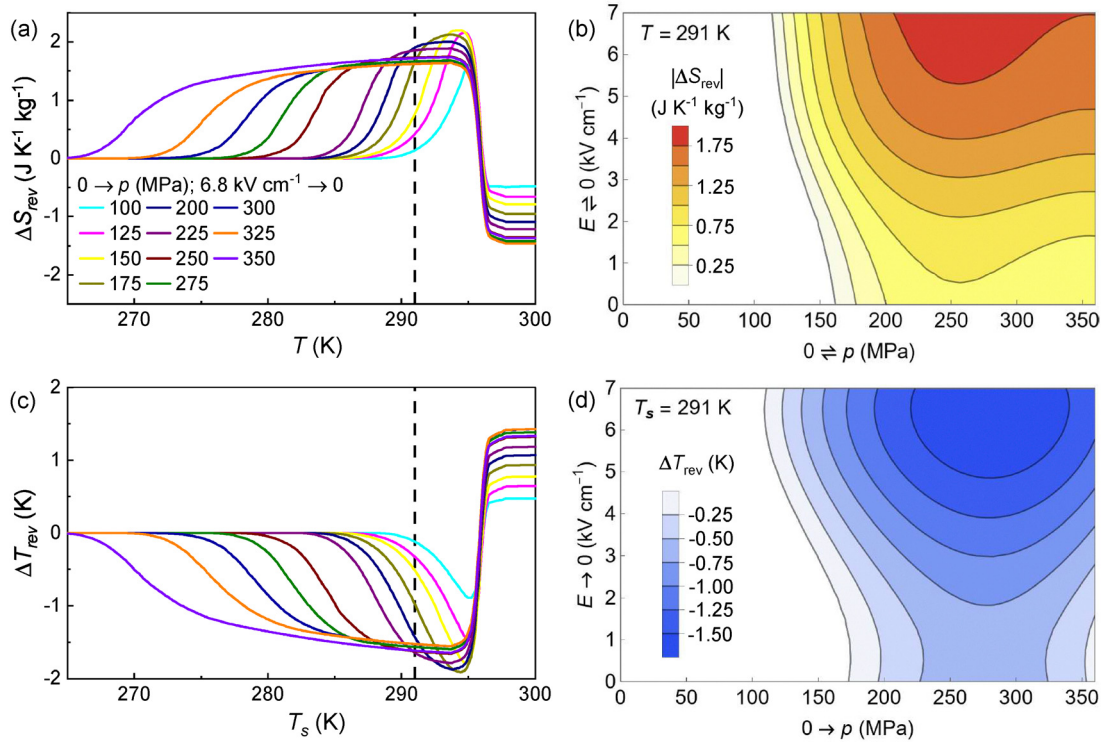

Fig. 4 (a) and (b) Reversible isothermal entropy changes and (c), (d) reversible adiabatic temperature changes as a function of the pressure increase and electric field decrease, (a), (c) as a function of temperature for $\Delta E = -6.8$ kV cm^{-1} and (b), (d) as a function of the field changes at $T = 291$ K. Dashed lines in panels (a) and (c) indicate $T = 291$ K.

Δp and no reversible EC effects can be obtained below ~300 K for any ΔE. Instead, by combining changes in the two fields, reversible multicaloric effects can then be obtained at any temperature. For instance, two reversible cycles (solid and dashed lines), which can each be traversed in both directions, are depicted on an isothermal surface at $T = 295$ K. In the B ↔ D cycle (solid line), the exothermic transition takes place at B ($p = 0$, $E = 5.7$ kV cm^{-1}, blue circle), which can be achieved from A by increasing the electric field at $p = 0$ or by decreasing pressure from C at $E = 5.7$ kV cm^{-1}. Notice that if, after completing this transition, the reverse path were performed (B → A or B → C), the material would not return to the initial phase due to the transition hysteresis because the endothermic transition surface would not be crossed. Therefore, the cycle would be irreversible. However, this cycle can become reversible if the system is brought to D ($p = 85$ MPa, $E = 0$), where it

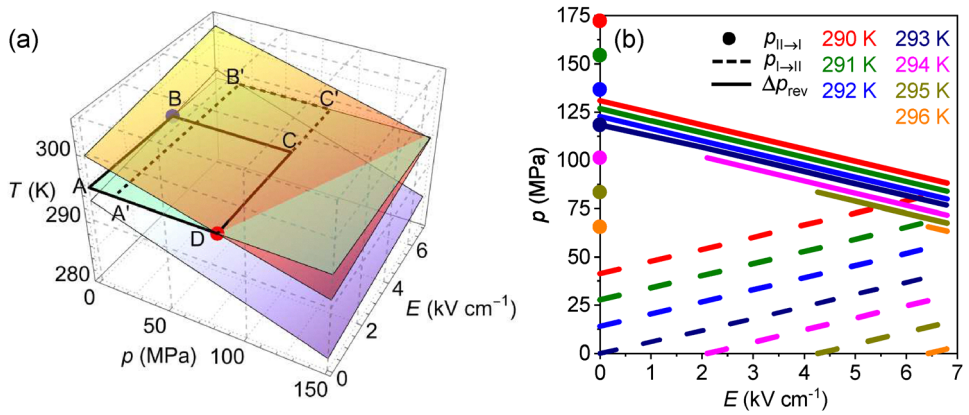

Fig. 5 (a) Reversible isothermal paths (black solid and dashed lines) in the $T(p,E)$ phase diagram. The yellowish surface and red circle indicate endothermic transitions, bluish surface and blue circle indicate exothermic transitions and the green surface indicates the isothermal surface at 295 K. (b) Circles and dashed lines indicate the endothermic transition pressure in the absence of applied electric field, and the exothermic transition pressure as a function of the electric field, respectively, for different temperatures. Solid lines display the minimum pressure change required to obtain reversible effects as a function of the applied electric field change, for different temperatures, calculated as the difference between circles and dashed lines.

would undergo the endothermic transition. This can be achieved by travelling through either A or C or, actually, through any arbitrary path. Generally, the most efficient path would be to return to A because this path minimizes the time of application of electric field, which is always energetically costly due to the normal operation of power suppliers even in the ideal case of the lack of leaks associated with local electrical breakdown.

On the other hand, other cycles entailing different field changes can also be designed. For instance, in the cycle B′ ↔ D, the exothermic transition takes place at B′ (p = 20 MPa, E = 6.8 kV cm^{-1}), whereas the endothermic transition takes place at D (p = 85 MPa, E = 0). Therefore, comparing both cycles, B ↔ D entails changes of Δp = 85 MPa and ΔE = 5.7 kV cm^{-1}, whereas B′ ↔ D entails changes of Δp = 65 MPa and ΔE = 6.8 kV cm^{-1}. Therefore, a reduction in Δp can be achieved by increasing ΔE. The relationship between these two quantities to obtain reversible cycles is shown for different temperatures in Fig. 5(b). A color refers to a single temperature. The endothermic transition is assumed to take place always at p_{endo} and E = 0 and is indicated by the symbol. The dependence of the exothermic transition pressure p_{exo} on the electric field change is indicated by dashed lines and the minimum pressure change required for reversible caloric effects, $\Delta p_{rev} = p_{endo} - p_{exo}$, is indicated by solid lines. As expected, Δp_{rev} decreases with increasing E. In the general case, the best choice should not only take into account the material's efficiency in terms of the balance between electrical and mechanical work but also other considerations come into play, both at the material level (*e.g.* reduction of electrical breakdown fields) and at the device level (*e.g.* work recovery, reduction of pressure wall thickness, safety).

In practice, multicaloric effects demand relatively large transition sensitivity to both fields, which depends on the ratio between changes in volume or polarization and entropy according to the Clausius–Clapeyron equation. In turn, thin films typically exhibit higher electrical breakdown fields but undergo mechanical breakdown under lower pressures than bulk ceramics.[53] Therefore, a feasible combination of the field strength and the transition sensitivity should be assessed in a case-by-case scenario. For instance, if a particular material requires moderate changes in both fields (∼100 kV cm^{-1}, ∼100 MPa), as it might be the case for some hybrid organic–inorganic ferroelectric perovskites,[54] thick films might be the best material shaping. Typical lead-containing compounds, such as PST, require lower electric fields and higher pressures for which bulk ceramics should be suitable. Instead, the electrocaloric strength of ferroelectric polymers and ferroelectric plastic crystals is smaller, requiring larger electric fields, and therefore thin films should be considered in those cases. Finally, it is worth mentioning here supertetragonal $BiFe_{1-x}Co_xO_3$ solid solutions which might require small changes in both electric field and pressure,[55] thus allowing for multiple material shapings.

4 Conclusions

Conjoined changes in volume and polarization at ferroelectric phase transitions are promising for multicaloric effects under simultaneous shifts in electric field and hydrostatic pressure but this is still terra incognita. In this work, the prototypical ferroelectric compound lead scandium tantalate is subjected to these two fields in unprecedented experiments of calorimetry and dielectric spectroscopy. Using the quasi-direct method, we found that the simultaneous application of the two fields multiplies the caloric response in relation to that obtained with a single field change. As an example, the response under decompression from 250 MPa down to atmospheric pressure is tripled if an electric-field shift of ∼6 kV cm^{-1} is simultaneously applied. Conversely, reversible caloric effects driven by low electric fields can only be realized if a pressure change is also applied. On the other hand, if a constant pressure is considered, electrocaloric effects can be shifted to match the range required for air conditioning and household refrigeration, from below to room temperature. We have also provided physical information about the thermodynamics of the phase transition in the multidimensional phase space, with insights on the phase diagram and cross-coupling between non-conjugated quantities.

Our study is a proof-of-concept of the experimental viability and impact on the multicaloric performance driven by shifts in pressure and electric field. Moreover, as our results are demonstrated on the most widely used solid-state cooling agent in electrocaloric prototypes, they should also provide opportunities for innovative device designs. Yet, the extensive and varied family of ferroelectric materials offers considerable room for improvement which, inspired by our findings, should encourage similar studies in other compounds of the same kind.

Conflicts of interest

There are no conflicts to declare.

Data availability

The data supporting this article have been included as part of the ESI.†

Acknowledgements

This work was supported by SGR-00343 Project (Catalonia), by Grant PID2023-146623NB-I00 funded by MICIU and by ERDF/EU, and is part of the Maria de Maeztu Units of Excellence Programme CEX2023-001300-M/funded by MCIN/AEI/10.13039/501100011033. This project has received funding from the European Unions Horizon 2020 research and innovation programme under the Marie Skłodowska-Curie grant agreement no 101107561. J.-Ll. T. is grateful to the ICREA Academia program. M. R. is a Serra Húnter fellow. H. U., S. D. and I. G. acknowledge the financial support of the Slovenian Research and Innovation Agency for the research funding (no. J2-60035, N2-0212, and P2-0105 and Young Researcher Funding). The assistance of Brigita Kmet and Jena Cilensek is gratefully acknowledged.

Notes and references

1 X. Moya and N. Mathur, *Science*, 2020, **370**, 797–803.
2 E. Stern-Taulats, T. Castán, L. Mañosa, A. Planes, N. D. Mathur and X. Moya, *MRS Bull.*, 2018, **43**, 295–299.
3 A. Planes, T. Castan and A. Saxena, *Philos. Mag.*, 2014, **94**, 1893–1908.
4 A. Aznar, P. Lloveras, M. Barrio, P. Negrier, A. Planes, L. Mañosa, N. D. Mathur, X. Moya and J.-L. Tamarit, *J. Mater. Chem. A*, 2020, **8**, 639–647.
5 J. Liu, T. Gottschall, K. P. Skokov, J. D. Moore and O. Gutfleisch, *Nat. Mater.*, 2012, **11**, 620–626.
6 H. Hou, S. Qian and I. Takeuchi, *Nat. Rev. Mater.*, 2022, **7**, 633–652.
7 Y. Sun, Z. Arnold, J. Kamarad, G.-J. Wang, B.-G. Shen and Z.-H. Cheng, *Appl. Phys. Lett.*, 2006, **89**, 172513.
8 L. Morellon, Z. Arnold, C. Magen, C. Ritter, O. Prokhnenko, Y. Skorokhod, P. Algarabel, M. Ibarra and J. Kamarad, *Phys. Rev. Lett.*, 2004, **93**, 137201.
9 T. Samanta, D. L. Lepkowski, A. U. Saleheen, A. Shankar, J. Prestigiacomo, I. Dubenko, A. Quetz, I. W. Oswald, G. T. McCandless and J. Y. Chan, *et al.*, *Phys. Rev. B: Condens. Matter Mater. Phys.*, 2015, **91**, 020401.
10 S. Patel, A. Chauhan, R. Vaish and C. S. Lynch, *J. Am. Ceram. Soc.*, 2017, **100**, 4902–4911.
11 T. Gottschall, A. Gràcia-Condal, M. Fries, A. Taubel, L. Pfeuffer, L. Mañosa, A. Planes, K. P. Skokov and O. Gutfleisch, *Nat. Mater.*, 2018, **17**, 929–934.
12 A. Gràcia-Condal, E. Stern-Taulats, A. Planes and L. Mañosa, *Phys. Rev. Mater.*, 2018, **2**, 084413.
13 X. Cheng, Y. Li, D. Zhu, M. Li and M. Feng, *J. Mater. Sci.*, 2020, **55**, 8802–8813.
14 E. Stern-Taulats, T. Castán, A. Planes, L. H. Lewis, R. Barua, S. Pramanick, S. Majumdar and L. Mañosa, *Phys. Rev. B*, 2017, **95**, 104424.
15 P. Lloveras, E. Stern-Taulats, M. Barrio, J.-L. Tamarit, S. Crossley, W. Li, V. Pomjakushin, A. Planes, L. Mañosa and N. Mathur, *et al.*, *Nat. Commun.*, 2015, **6**, 8801.
16 S. Crossley, W. Li, X. Moya and N. Mathur, *Philos. Trans. R. Soc., A*, 2016, **374**, 20150313.
17 V. Bondarev, E. Mikhaleva, M. Gorev and I. Flerov, *J. Alloys Compd.*, 2022, **892**, 162130.
18 X. Moya, E. Stern-Taulats, S. Crossley, D. González-Alonso, S. Kar-Narayan, A. Planes, L. Mañosa and N. D. Mathur, *Adv. Mater.*, 2013, **9**, 1360–1365.
19 E. Stern-Taulats, P. Lloveras, M. Barrio, E. Defay, M. Egilmez, A. Planes, J.-L. Tamarit, L. Mañosa, N. Mathur and X. Moya, *APL Mater.*, 2016, **4**, 091102.
20 S. Patel, A. Chauhan, R. Vaish and P. Thomas, *Appl. Phys. Lett.*, 2016, **108**, 072903.
21 Q. Li, G. Zhang, X. Zhang, S. Jiang, Y. Zeng and Q. Wang, *Adv. Mater.*, 2015, **27**, 2236–2241.
22 A. Salvatori, D. Aguilà, G. Arom, L. Mañosa, A. Planes, P. Lloveras, L. C. Pardo, M. Appel, G. F. Nataf and F. Giovannelli, *et al.*, *J. Mater. Chem. A*, 2023, **11**, 12140–12150.
23 Y. Liu, G. Zhang, Q. Li, L. Bellaiche, J. F. Scott, B. Dkhil and Q. Wang, *Phys. Rev. B*, 2016, **94**, 214113.
24 S. Lisenkov, B. Mani, C.-M. Chang, J. Almand and I. Ponomareva, *Phys. Rev. B*, 2013, **87**, 224101.
25 N. Shorrocks, R. Whatmore and P. Osbond, *Ferroelectrics*, 1990, **106**, 387–392.
26 L. Shebanovs, K. Borman, W. Lawless and A. Kalvane, *Ferroelectrics*, 2002, **273**, 137–142.
27 Y. Nouchokgwe, P. Lheritier, C.-H. Hong, A. Torelló, R. Faye, W. Jo, C. R. Bahl and E. Defay, *Nat. Commun.*, 2021, **12**, 3298.
28 A. Torelló, P. Lheritier, T. Usui, Y. Nouchokgwe, M. Gérard, O. Bouton, S. Hirose and E. Defay, *Science*, 2020, **370**, 125–129.
29 J. Li, A. Torelló, V. Kovacova, U. Prah, A. Aravindhan, T. Granzow, T. Usui, S. Hirose and E. Defay, *Science*, 2023, **382**, 801–805.
30 J. P. Perdew, K. Burke and M. Ernzerhof, *Phys. Rev. Lett.*, 1996, **77**, 3865.
31 G. Kresse and J. Furthmüller, *Phys. Rev. B*, 1996, **54** 11169.
32 G. Kresse and D. Joubert, *Phys. Rev. B*, 1999, **59**, 1758.
33 P. E. Blöchl, *Phys. Rev. B*, 1994, **50**, 17953.
34 C. Cazorla and J. Íniguez, *Phys. Rev. B*, 2013, **88**, 214430.
35 C. Cazorla, O. Diéguez and J. Íñiguez, *Sci. Adv.*, 2017, **3**, e1700288.
36 C. Cazorla, *Appl. Phys. Rev.*, 2019, **6**, 041316.
37 C. Menéndez and C. Cazorla, *Phys. Rev. Lett.*, 2020, **125**, 117601.
38 C. Menéndez, D. Chu and C. Cazorla, *npj Comput. Mater.*, 2020, **6**, 76.
39 A. Togo, *J. Phys. Soc. Jpn.*, 2023, **92**, 012001.
40 N. Setter and L. Cross, *J. Appl. Phys.*, 1980, **51**, 4356–4360.
41 C. Stenger and A. Burggraaf, *Phys. Status Solidi A*, 1980, **61**, 653–664.
42 C. Stenger and A. Burggraaf, *Phys. Status Solidi A*, 1980, **61**, 275–285.
43 L. Shebanov, E. Birks and K. Borman, *Ferroelectrics*, 1989, **90**, 165–172.
44 A. Paul, J. Sun, J. P. Perdew and U. V. Waghmare, *Phys. Rev. B*, 2017, **95**, 054111.
45 P. Woodward and K. Baba-Kishi, *Appl. Crystallogr.*, 2002, **35**, 233–242.
46 S. Crossley, R. Whatmore, N. Mathur and X. Moya, *APL Mater.*, 2021, **9**, 010701.
47 S. Kustov, D. Salas, E. Cesari, R. Santamarta and J. Van Humbeeck, *Acta Mater.*, 2012, **60**, 2578–2592.
48 J.-H. Ko, F. Jiang, S. Kojima, T. Shaplygina and S. Lushnikov, *J. Phys.: Condens. Matter*, 2001, **13**, 5449.
49 Y. Nouchokgwe, P. Lheritier, T. Usui, A. Torello, A. El Moul, V. Kovacova, T. Granzow, S. Hirose and E. Defay, *Scr. Mater.*, 2022, **219**, 114873.
50 F. Chu, G. R. Fox and N. Setter, *J. Am. Ceram. Soc.*, 1998, **81**, 1577–1582.
51 E. Stern-Taulats, P. Lloveras, M. Barrio, J.-L. Tamarit, A. Planes, L. Mañosa, R. Whatmore, N. Mathur and

X. Moya, *arXiv*, 2020, preprint, arXiv:2010.15705, DOI: 10.48550/2010.15705.
52 L. Mañosa, E. Stern-Taulats, A. Gràcia-Condal and A. Planes, *J. Phys.: Energy*, 2023, **5**, 024016.
53 M. Valant, *Prog. Mater. Sci.*, 2012, **57**, 980–1009.
54 Y. Lin, C. Chai, Z. Liu, J. Wang, S. Jin, Y. Yang, Y. Gao, M. Hao, X. Li and Y. Hou, *et al.*, *Nat. Commun.*, 2025, **16**, 4009.
55 C. Menéndez, R. Rurali and C. Cazorla, *Phys. Chem. Chem. Phys.*, 2023, **25**, 17450–17459.